Structural, electronic, and vibrational properties of (4,4) picotube crystals

M. Machón,[1] S. Reich,[2] J. Maultzsch,[1] H. Okudera,[3] A. Simon,[3] R. Herges,[4] and C. Thomsen[1]
[1]*Institut für Festkörperphysik, Technische Universität Berlin, Hardenbergstrasse 36, 10623 Berlin, Germany*
[2]*Department of Engineering, University of Cambridge, Trumpington Street, Cambridge CB2 1PZ, United Kingdom*
[3]*Max-Planck-Institut für Festkörperforschung, Heisenbergstraße 1, D-70569 Stuttgart, Germany*
[4]*Institut für Organische Chemie, Universität Kiel, Otto-Hahn-Platz 4, 24098 Kiel, Germany*
(Received 2 June 2005; revised manuscript received 10 August 2005; published 6 October 2005)

The picotube molecule is a highly symmetric hydrocarbon, closely related to a very short (4,4) carbon nanotube. We present a thorough experimental and theoretical study of the physical properties of picotube crystals. In x-ray diffraction experiments we find the picotube molecules to display D_{2d} symmetry. We identify the most intense Raman peaks as A_1 modes with polarization-dependent Raman measurements. *Ab initio* calculations of the structural, electronic, and vibrational properties of picotubes are in excellent agreement with our experiments. We assign the measured vibrations to displacement eigenvectors including those analogous to the nanotube high-energy mode, the *D* mode, and the radial-breathing mode.

DOI: 10.1103/PhysRevB.72.155402 PACS number(s): 33.20.Fb, 33.15.Bh, 31.15.Ar, 78.30.Na

I. INTRODUCTION

The discovery of fullerenes and carbon nanotubes greatly stimulated the interest of the physics community in carbon materials. In 1996 a new, highly symmetric hydrocarbon was synthesized and given the name picotube.[1] The name refers to the resemblance of the molecule to a very short (4,4) nanotube. A picotube represents a crucial step toward chirality selective growth of carbon nanotubes with chemical methods. The electric and optical properties of nanotubes depend on the diameter and chirality, so that a precise control of their production is desirable.[2] The physical methods used for nanotube synthesis rely mainly on self-organization with a carbon plasma as starting point. Calculations of the nanotube folding energy show a smooth dependence on the nanotube diameter in agreement with the uniform chirality distributions measured up to now.[3–6] In contrast, organic chemistry can control the breaking and formation of single bonds with great accuracy. Controlled switching between well-defined geometries is possible representing a promising way of achieving the goal of chirality specific growth. The synthesis of picotube molecules is a good example of this. These crystals are currently the closest available to a monochiral nanotube crystal.[5,7,8]

Another interesting feature of the picotubes is their size. With a diameter of 5.4 Å they are closely related to the smallest nanotubes available.[9] The properties of these very small nanotubes can differ strongly from those of their bigger counterparts and are subject of intense study.[10–14] The curvature of the nanotube walls has important effects on the electronic and optical properties of nanotubes and cannot be derived from graphene.[12–17] Nevertheless, much of the understanding of carbon nanotubes has been derived from the known properties of graphene.[2] This approach has the advantage of explaining many regularities of the properties of nanotubes, but it breaks down when the curvature starts to play an important role. Picotube crystals can serve as a complementary approach to the understanding of carbon nanotubes, including the curvature of the walls. For small nanotubes, a rehybridization of the σ and π orbitals has been predicted and observed indirectly through photoluminescence and resonant Raman measurements.[5–7,13,16–19] The lower symmetry restriction in the picotube makes this effect visible in the molecular structure, where typical sp^3 angles are found (see Sec. III A).

In this paper we present a study on the structure, electronic properties, and vibrations of picotube crystals. The atomic structure was obtained with x-ray analysis. The picotube crystals belong to the C_{2h} symmetry group, whereas the picotube molecule is best described by D_{2d} symmetry. Calculations of the electronic properties of the picotube molecules are presented. We show polarization-dependent micro-Raman spectroscopy measurements. We obtained the symmetry of the most intense Raman modes and discuss the interaction strength of the molecules in the crystal. We assign the measured modes to atomic displacement patterns by comparing the measurements with *ab initio* calculations. We identify the counterparts of both the characteristic Raman modes of carbon nanotubes and the sp^3-like modes typical for small tubes with strong wall curvature.

This paper is organized as follows. We first describe the experimental and computational methods in Sec. II. In Sec. III we present the structure of picotube crystals as measured with x-ray diffraction. We compare with *ab initio* calculations for an isolated molecule. The electronic properties of the molecule are discussed in Sec. IV and compared with calculations for carbon nanotubes. In Sec. V we move to Raman measurements of picotube crystals. Measurements of the polarization dependence of the intensities allow us to obtain the symmetry of most intense peaks. An assignment of the Raman modes to atomic displacements based on *ab initio* calculations is presented in Sec. V C. Nanotube-typical modes like the radial-breathing mode, the high-energy mode, and the *D* mode are identified,[2] together with sp^3-like modes among others.

II. EXPERIMENTAL AND COMPUTATIONAL DETAILS

Picotube crystals have a characteristic flat shape. The longest edge is typically a few hundredths of micrometers long. They are transparent to the eye and easily break into pieces when pressed with a needle. The picotube molecules are synthesized by ring-expanding metathesis of tetradehydrodianthracene. The exact procedure can be found in Ref. 1.

Two different samples were used for the two experiments. The x-ray sample was prepared by placing a small vial of a homogeneous solution of the picotube in carbon disulfide into a larger flask with acetonitrile (diffusion method). The crystal was measured on an image plate diffraction system diffractometer (IPDS I) at 173 ± 2 K using graphite-monochromated Mo K_α radiation with $\lambda=0.710\,73$ Å. Crystallographic data for the measured structure have been deposited at the Cambridge Crystallographic Data Center (deposition number CCDC 273647) and can also be found in the supplementary materials Ref. 20.

The Raman sample was prepared by purification by high-performance liquid chromatography on a silica gel column with hexane-dichloromethane 2:1 and crystallized from a solution in pentane-dichloromethane (1:1). Micro-Raman spectra were recorded in backscattering geometry using a single-grating spectrometer[21] and an excitation wavelength of 633 nm. Our experimental setup had a resolution of $3-4$ cm^{-1} (full width at half maximum). Three inequivalent surfaces of the same crystal were measured. For the polarization-dependent experiments we rotated the sample under parallel and crossed polarization of the incoming and outgoing light.

Ab initio calculations were performed with the SIESTA code.[22,23] The local-density approximation was used for the exchange-correlation functional as parametrized by Perdew and Zunger.[24] The core electrons were replaced by nonlocal, norm-conserving pseudopotentials.[25] A double-ζ singly polarized basis set of localized atomic orbitals was used for the valence electrons. The cutoff radii were determined from an energy shift of 50 meV by localization.[26] For calculation of the picotube molecule we used a grid cutoff of $\approx$100 Ry in real space ($\approx$200 Ry for the calculation of the vibrations). Since SIESTA uses periodic boundary conditions, the molecule was placed in a cubic cell with side length of 25 Å to avoid interaction between the images. The parameters used for the nanotube calculations can be found elsewhere.[13] The structures were relaxed until the forces were smaller than 0.04 eV/Å. The calculation of the vibrational modes was performed with the method of finite differences.

III. STRUCTURAL PROPERTIES

A. Single molecules: X-ray scattering and *ab initio* calculations

Figure 1 shows the structure of a picotube ($C_{56}H_{32}$) as determined by x-ray diffraction. The molecule shows very small deviations from D_{2d} ($\bar{4}2m$) symmetry, in good agreement with infrared measurements[27] and density functional theory calculations (see Sec. III A and Ref. 27). The symmetry operations of the D_{2d} group are indicated in the figure: twofold rotation (C_2) and fourfold rotatory reflection (S_4) about the main axis; twofold rotation (C_2') about two axes perpendicular to the primary axis; reflection in two diagonal (σ_d) planes.

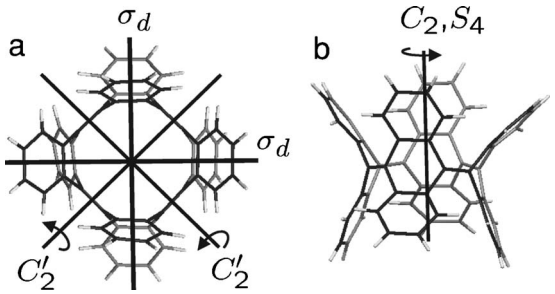

FIG. 1. (a) Top view of a picotube molecule from the x-ray measured crystal. Black (dark gray) carbon-carbon bonds are in the foreground (background) of the picture. Light gray atoms are hydrogen. Two twofold rotation axes (C_2') and two reflection planes (σ_d) are shown. (b) Side view of the same molecule. The main rotation axis is indicated (C_2, S_4).

The picotube molecule is closely related to the (4,4) armchair nanotube [see Fig. 2(a)]. The unit cell of a nanotube repeats periodically along the direction of its axis. Therefore it is treated as a one-dimensional solid rather than as a molecule. Cutting a section of three unit cells of a (4,4) nanotube [including three hexagons along the nanotube axis as indicated by the arrow in Fig. 2(a)] and opening the walls into four wings, yields a molecule with D_{4h} ($4/mmm$) symmetry [Fig. 2(c)], including fourfold rotation and inversion. In the actual structure, two of the wings of the molecule tend to close towards the main rotational axis (C_2), and two tend to bend away from it, complementarily on the lower side [compare Figs. 2(b) and 2(c)]. The fourfold rotation symmetry is

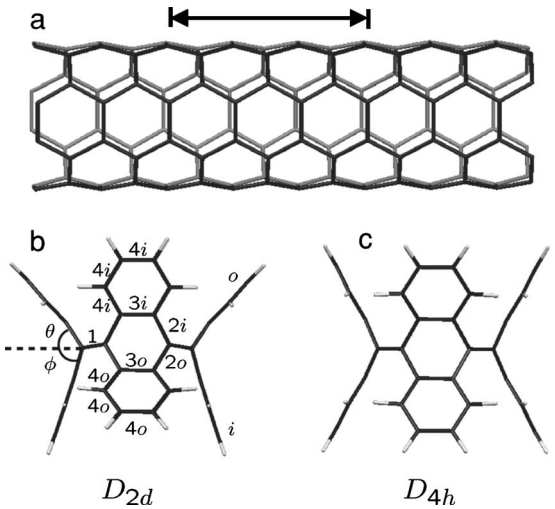

FIG. 2. (a) Structure of a (4,4) nanotube (gray bonds are in the background of the picture). (b) *Ab initio* calculated structure of the picotube molecule with D_{2d} ($\bar{4}2m$) symmetry and parameter definition for Table I. We denote the wings bending inward, i.e., toward the main rotational axis, as i, and those bending outward as o. Note the absence of inversion symmetry due to the asymmetry of the i and o wings of the molecule. (c) Idealized picotube geometry with D_{4h} ($4/mmm$) symmetry including inversion symmetry.

TABLE I. Structural parameters of the picotube (PT) molecules as measured by x-ray diffraction and calculated with *ab initio* methods. The notation corresponds to Fig. 2(b). In the last column the corresponding parameters of a calculated (4,4) nanotube (NT) are shown for comparison. The experimental parameters are mean values of symmetry-equivalent bonds.

		PT (expt.)	PT (calc.)	(4,4) (calc.)
Diameter (Å)		5.4	5.4	5.5
C-C bond length (Å)	1	1.36	1.37	1.43
	2*i*	1.51	1.49	1.43
	2*o*	1.49	1.48	1.43
	3*i*	1.42	1.43	1.43
	3*o*	1.41	1.42	1.43
	4*i*	1.39	1.40	1.43
	4*o*	1.39	1.40	1.43
C-H bond length (Å)		0.99	1.11	
C-C-C angles	2*i*-2*o*	108	109	119
	1-2*i*	126	126	118
	1-2*o*	126	125	118
Wing angle	θ	51	51	
	ϕ	70	73	

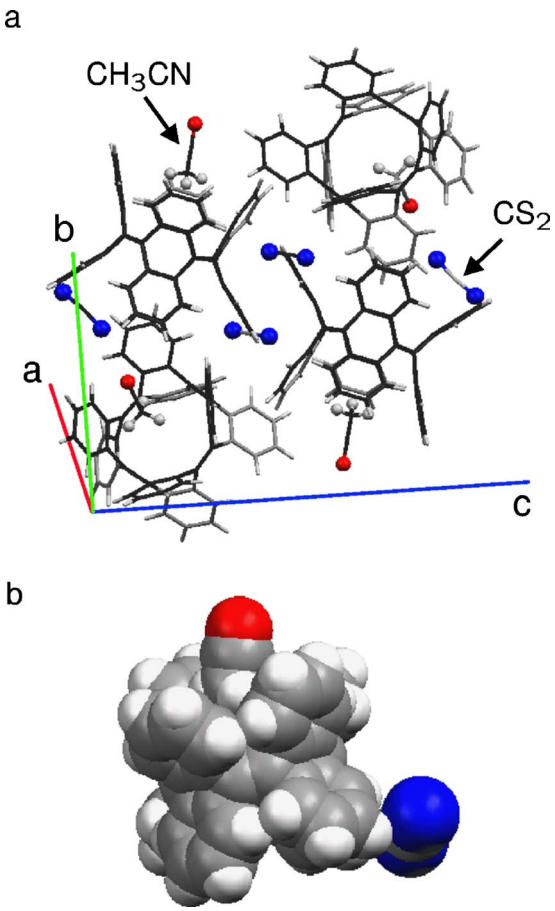

FIG. 3. (Color online) (a) Unit cell of the picotube crystal measured with x-ray diffraction. Carbon-carbon bonds in the foreground (background) are shown in black (dark gray). Light gray atoms are hydrogen, red nitrogen, and blue sulfur. For clarity, the non-carbon atoms of the CS_2 and CH_3CN molecules are represented as balls. The unit cell includes four $C_{56}H_{32}$ (picotube) molecules, four CS_2, and four CH_3CN molecules. Two of the picotubes are seen from the top and two from the side. Note the two parallel picotube wings in the center of the unit cell. (b) Space filling plot of the formula unit including one picotube, a CS_2 molecule, and a CH_3CN molecule, which has its CH_3 group inside the picotube.

lowered to a rotary reflection, i.e., a fourfold rotation followed by a horizontal mirror operation ($\sigma_h C_4 = S_4$). The resulting group is D_{2d}. The inversion symmetry is broken, which has important effects on the Raman selection rules (see Sec. V). This symmetry lowering is due to the repulsion between the neighboring wings.

We performed *ab initio* calculations of the structure of the picotube and found two equivalent minima of the total energy corresponding to the D_{2d} structure shown in Fig. 2(b), separated by a maximum corresponding to a D_{4h} symmetry [Fig. 2(c)]. The energy difference of 300 meV allows a conformational motion between the two equivalent minima in agreement with the calculations of Herges *et al.*[27] In Table I the structural parameters are shown for both the measured and the calculated picotube structures, as well as for a (4,4) single-walled nanotube. The agreement between the experimental and theoretical data for the picotube is excellent. Note that the calculation corresponds to an isolated molecule, whereas the measurements were performed in a crystal. The good agreement suggests a low interaction between the molecules in the crystal and a high stability of the molecule.

In the (4,4) nanotube, all carbon bonds have a similar length halfway in between a typical single and double bond length, consistent with delocalized electronic states. In the picotube, the bonds in the middle ring [denoted as bond 1 in Fig. 2(b) and in Table I] shrink toward the typical C-C double-bond length of 1.35 Å, whereas the neighboring bonds (2*i* and 2*o*) are longer than the delocalized carbon bonds. A similar effect is found for polycyclic aromatic hydrocarbons. These molecules are similar to unrolled picotubes of different sizes and shapes. They have unequal C-C bond lengths in contrast to the bonds of graphite, which are equivalent by symmetry.[28] Remarkably, the bond angle denoted as 2*i*-2*o* in the table is 109°, which is expected for sp^3 hybridization. All other angles are close to the sp^2 value of 120°. Similar angles are found for the metastable structure with D_{4h} symmetry.

In contrast to graphite, where the σ and π orbitals are orthogonal, the curvature of the picotube central ring and nanotube wall enforces an interaction of these orbitals. This has important consequences for the electronic and optical properties of carbon nanotubes, e.g., turning tubes that are expected to be semiconducting from zone folding into metals.[13,16,17] In armchair nanotubes such small angles between bonds have only been obtained in calculations of 3-Å-diameter nanotubes.[29] The observed angle of 109° is a direct consequence of the rehybridization of σ and π orbitals due to the wall curvature.

TABLE II. Unit cell vectors and angles of the picotube crystal measured with x-ray diffraction.

a	b	c	α	β	γ
12.470 Å	16.030 Å	20.950 Å	90°	98.13°	90°

B. Picotube crystal: X-ray scattering

In Fig. 3(a) the structure of the picotube crystal obtained from x-ray analysis is shown. The unit cell is monoclinic, space group $C_{2h}^5(P2_1/c)$, with the parameters given in Table II. This symmetry group includes inversion symmetry, a glide plane, and a twofold screw axis. The crystal contains per formula unit one picotube ($C_{56}H_{32}$), a carbon disulfide molecule (CS_2), an acetonitrile molecule (CH_3CN), and four formula units per unit cell. The four picotubes are arranged in pairs, with an angle of 74° between the main rotational axes of the molecules. Each picotube has three of its hexagonal wings confronted to a wing of a neighboring molecule. In this way, two carbon hexagons from the wings of two different molecules are parallel to each other at a distance of about 3.6 Å; see, e.g., the two wings in the center of Fig. 3(a). The distance between the wings is close to the graphite interlayer distance, thus lowering the energy of the system via van der Waals interaction. Interestingly, this situation is favored by the D_{2d} symmetry of the molecule and may be the reason for the good agreement of the calculated structure of a single molecule with the molecular structure in the crystal. In Fig. 3(b) a space filling plot of the formula unit is shown. The acetonitrile molecule has its CH_3 group inside the picotube molecule.

Until now we discussed the structural properties of picotube molecules and crystals. In the following, we discuss the electronic and vibrational properties of our samples.

IV. ELECTRONIC PROPERTIES

In this section we will show theoretical results on the electronic properties of picotube molecules and compare them to the properties of carbon nanotubes. On the left of Fig. 4(a) we show the calculated density of states (DOS) for the picotube. The highest and lowest occupied molecular orbitals (HOMO and LUMO, respectively) are separated by 2.3 eV. Measurements of absorption of picotubes in solution show the absorption with the longest wavelength at 300 nm corresponding to an energy of ≈4.1 eV (Ref. 1). This is higher than our theoretical prediction. However, it is known that the density functional theory underestimates the band and HOMO-LUMO gaps,[30] in particular, for molecules where the structure of the ground and excited states often differs.[28,31] The picotube has a very large HOMO-LUMO gap when compared to the band gap of carbon nanotubes, which comes from the molecular character of the picotube.

In Figs. 4(b) and 4(c) the calculated DOS and the band structure of a (4,4) nanotube can be seen. This nanotube is a metal, with its bands crossing close to two-thirds of the Brillouin zone (label K).[32] To compare the DOS of the (4,4) nanotube to that of the picotube molecule, we extract from

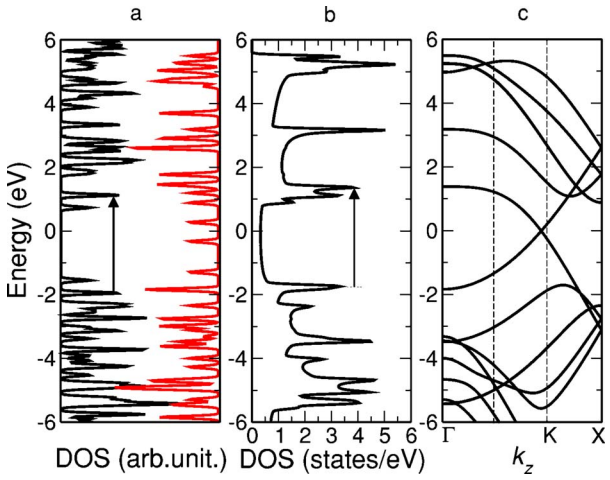

FIG. 4. (Color online) (a) Calculated electronic density of states of the picotube. Left-hand side, black lines: full calculation. Right-hand side, red: density of states derived from the electronic band structure of the (4,4) nanotube. The arrow indicates the first optical transition for light polarized parallel to the main rotational axis of the molecule. (b) Calculated electronic density of states of a (4,4) carbon nanotube. The arrow indicates the first optical transition for light polarized parallel to the nanotube axis. (c) Calculated electronic band structure of a (4,4) carbon nanotube.

the band structure of the tube the states with k_z vectors compatible with a nanotube length of three unit cells. In this approximation we consider the two systems equal around their circumference, and we neglect the effect of the hydrogen atoms on the electronic band structure. The latter approximation is reasonable because the H-related states are ≈4 eV above and below the Fermi level.

The quantization condition along the nanotube axis is $k_z = n\pi/3a$, where n is integer and a is the unit cell length of the nanotube. The allowed k_z are the Γ and X points, the point at two-thirds of the Brillouin zone (which corresponds to the K point of graphite in the zone-folding scheme, and will be therefore denoted as the K point from now on) and the point halfway between Γ and K [see vertical dashed lines in Fig. 4(c)]. From the eigenenergies at these k points we calculated a nanotube-derived DOS, which is shown to the right in Fig. 4(a) [red (gray) lines]. Comparing with the DOS from the full calculation, we see that the energy difference between the HOMO and LUMO of the picotube is much larger than predicted by the zone-folding approach. However, the picotube gap is close to the so-called optical gap of the (4,4) nanotube, meaning the energy of the first optical transition. Comparing the lowest optical transitions for light polarized parallel to the main rotational axes of the picotube and nanotube [indicated with arrows in Figs. 4(a) and 4(b)], we find very similar transition energies.

We calculated the wave functions of the HOMO and LUMO of the picotube molecule, which can be seen in Figs. 5(c) and 5(a), respectively. In panels (b) and (d) the corresponding wave functions from the K point of the (4,4) nanotube are shown. In the central ring of the picotube, the wave functions are almost identical to those of the nanotube. Furthermore, the symmetry with respect to the σ_d reflection planes is the same. The parity with respect to these planes is

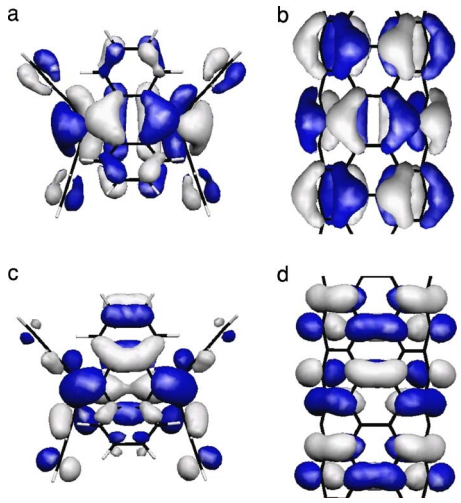

FIG. 5. (Color online) *Ab initio* calculated HOMO and LUMO wave functions for the picotube molecule and the (4,4) nanotube. The surfaces shown correspond to a probability amplitude of ±0.05. The two colors denote the different signs of the wave function. (a) LUMO of the picotube molecule, (b) LUMO of the infinite (4,4) nanotube, (c) HOMO of the picotube molecule, and (d) HOMO of the infinite (4,4) nanotube.

odd for the wave functions in Figs. 5(a) and 5(b) and even for 5(c) and 5(d). An electronic transition between HOMO and LUMO through absorption of light polarized along the axis of the molecule (with positive parity with respect to σ_d) is thus forbidden by symmetry. The first allowed optical transitions for light polarized along the main rotational axis of the picotube and (4,4) nanotube are indicated in Figs. 4(a) and 4(b), respectively. Note that the selection rules for light polarized perpendicularly to the axis are different. In this configuration the absorbed photon changes the parity of the electron.

There are also differences between the wave functions of the picotube and the nanotube. Comparing the HOMO of the picotube and the corresponding wave function of the nanotube, we see that—apart from the central ring—the electronic clouds are mainly concentrated in the wings denoted as *i* in Fig. 2. Due to the lower symmetry of D_{4h} compared to D_{2d} the wings are not equivalent by symmetry, but they separate in two groups (*i* and *o* as defined in Fig. 2). This lowers the interaction between the wings and contributes to the lowering of the symmetry from D_{4h} to D_{2d}.

V. VIBRATIONAL PROPERTIES

In the following we concentrate on the vibrational properties of the picotube molecules, starting with general properties of the vibrational spectrum. Polarization-dependent Raman measurements allow us to obtain the symmetries of the main peaks. With the help of *ab initio* calculations we are able to assign eigenvectors to the observed vibrational modes.

A. Raman spectrum

The picotube molecules ($C_{56}H_{32}$) have D_{2d} symmetry, as we found in the x-ray investigations (see Sec. III). All normal modes are expected to be Raman active from group theory.[33,34] If we restrict the analysis to the symmetric part of the Raman tensor (excluding thus the 33 A_2 modes), the dynamical representation can be decomposed as $33\,A_1 \oplus 33\,B_1 \oplus 33\,B_2 \oplus 132\,E$.

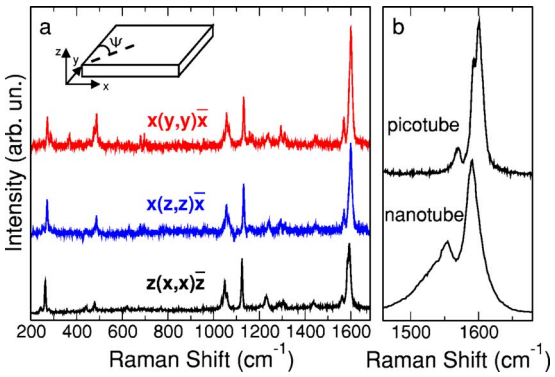

FIG. 6. (Color online) (a) Micro-Raman spectra of the picotube crystal with incident and scattered light parallel to the three inequivalent crystal edges. (Ref. 51). Inset: shape of the crystal and system of reference. (b) High-energy region of the measured Raman spectrum of a picotube crystal $[z(x,x)\bar{z}$, same as the black-line spectrum in (a)] and a sample of bundled nanotubes (mean diameter ≈1 nm), both excited at 633 nm.

In Fig. 6 we show three Raman spectra of a picotube crystal with polarization parallel to the three inequivalent crystal edges. The spectra are dominated by a feature at about 1600 cm^{-1}, typical for sp^2 carbon compounds. In this band, we can resolve two modes at 1601 and 1592 cm^{-1}, plus a less intense mode at 1569 cm^{-1}. The analysis of polarization-dependent Raman measurements suggests that, in fact, more than two modes give rise to this feature (see Sec. V B). In the range between 1000 and 1400 cm^{-1}, several modes are found. The single peak at 1131 cm^{-1} is the most intense one followed by a group of three modes at about 1050 cm^{-1}. In the low-energy region, features appear around 480 cm^{-1} and 280 cm^{-1}. In Sec. V B we summarize the measured frequencies for the most intense peaks in the range from 200 to 1700 cm^{-1} (see Table III).

The shape of the band at ca. 1600 cm^{-1} in the spectrum of the picotube crystal is very similar to the characteristic double-peak shape in the spectrum of single-walled nanotubes [see Fig. 6(b)]. In particular, the Raman spectra of isolated single-walled carbon nanotubes often look very similar to the picotubes high-energy modes except for slightly different frequencies.[35] The high-energy line shape has, however, a different origin for each system. The nanotube high-energy mode stems from two totally symmetric vibrational branches derived from the in-plane optical phonon of graphite (one branch in the case of achiral nanotubes).[36,37] The broad line shape, also found for isolated nanotubes, has its origin in a double-resonant process involving vibrational modes away from the Γ point ($q \neq 0$).[38–40] Such double-resonant processes are related to the electronic and vibrational dispersions of the nanotubes and are not expected from a molecule. In the picotube the Raman band comes from the several overlapping modes. The differences between the pico- and the nanotube's Raman spectra origi-

TABLE III. Observed frequencies, assigned symmetries, fitted Raman tensors, and character of the picotube phonon eigenvectors from *ab initio* calculations. We show the non-zero elements of the Raman tensor, normalized to r_{11} of the peak at 1601 cm^{-1}.

ω (cm^{-1})	Symmetry	Raman tensor	Eigenvector
1601	A_1	$r_{11}=r_{22}=1.00$ $r_{33}=-1.55$	Tangential C-C stretch
1592	A_1, B_2, E		Tangential C-C stretch
1569			Tangential C-C stretch
1445			
1313			
1294	A_1	$r_{11}=r_{22}=0.24$ $r_{33}=-0.63$	sp^3-like C-C stretch
1238			
1171	A_1	$r_{11}=r_{22}=0.10$ $r_{33}=-0.25$	
1158	A_1	$r_{11}=r_{22}=0.16$ $r_{33}=-0.35$	
1131	A_1	$r_{11}=r_{22}=0.58$ $r_{33}=-0.58$	C-C stretch
1066	A_1 or B_1		
1056	A_1 or B_1		
1042	A_1 or B_1		
488, 479, 473			Wing torsion Radial-axial
286, 272, 253			Hexagon libration Bending, breathing

nate from three sources. First, we have to take into account the different aspect ratio of picotubes and nanotubes. The large aspect ratio of nanotubes gives rise to the antenna effect,[41,42] which suppresses all nondiagonal contributions to the Raman tensors.[2,43] Only totally symmetric modes are observed in the Raman spectrum of nanotubes.[36,37,43,44] This is not expected for the picotubes because of their much lower aspect ratio. Second, for every Raman allowed branch of a (4,4) nanotube we can derive several Raman allowed picotube vibrational modes by applying the same zone-folding procedure to the nanotube vibrational bands as explained for the electronic bands in Sec. IV. Third, the lower symmetry of the picotube, for example the absence of inversion, allows more modes to be Raman active.

The *ab initio* calculations presented in Sec. V C indicate the mode at 1596 cm^{-1} as a possible analog of the *D* mode of carbon nanotubes. The energy of this Raman peak is much higher than the energy of the *D* mode in graphite or nanotubes. Symmetry and the calculated eigenvectors show that the 1596 cm^{-1} mode corresponds to the *K*-point TO mode of graphite (see Sec. V C and Fig. 9 for details).[28,31]

The third feature in the Raman spectra of single-walled nanotubes is the radial-breathing mode (RBM). The RBM is one of the Raman fingerprints of single-walled tubes, since it is absent in the spectra of graphite or multiwalled nanotubes.[45,46] It corresponds to an in-phase radial vibration of all atoms of the nanotube, with a small nonradial component.[4,47] For carbon nanotubes, the frequency of the radial-breathing mode depends inversely on the tube diameter.[6,18,48–50] We use the experimentally determined parameters from Telg *et al.*,[6] and obtain

$$\omega_{\mathrm{RBM}} = \frac{214}{d}\ \mathrm{cm^{-1}\,nm} + 19\ \mathrm{cm^{-1}} = 408\ \mathrm{cm^{-1}} \qquad (1)$$

for the (4,4) nanotube with diameter 0.55 nm. The *ab initio* calculated radial-breathing mode of the (4,4) nanotube is found at 413 cm^{-1} in very good agreement with Eq. (1). Our *ab initio* calculations of the picotube's vibrational properties show, however, a breathinglike mode at much lower frequency than expected from Eq. (1), closer to the measured peaks at $\approx$270 cm^{-1}. This lower frequency is due to the lower symmetry of the picotube (see Sec. V C for details).

Let us now look back at the x-ray structure of the picotube crystal shown in Fig. 3. The symmetry of the picotube is D_{2d}. Although this is lowered to C_{2h} in the crystal, we find two planes that are structurally almost identical (for example the one shown in the figure, the second found by turning the unit cell by 90° about the *c* axis), whereas the third perpendicular plane shows a different configuration. Figure 6 displays Raman spectra taken with light polarized parallel to the three inequivalent edges of a single picotube crystal. Clearly, two of the spectra are practically the same $[x(y,y)\bar{x}$ and $x(z,z)\bar{x}]$, while the $z(x,x)\bar{z}$ differs from the other two.[51] Compare, for example, the shape of the double peak at $\approx$1600 cm^{-1} or the group at $\approx$480 cm^{-1}. In the following we discuss angle-resolved polarized Raman spectra and use them to assign the symmetry of the vibrational modes.

B. Polarized Raman measurements

To assign the symmetry of the vibrational modes we performed polarization-dependent Raman measurements. Figure 7(a) shows the measured Raman intensity as function of the angle ψ between the excitation polarization and the *y* direction for the mode at 1601 cm^{-1}. At first sight, the polarization dependence seems to show an A_1 behavior. The Raman intensity in parallel polarization (closed symbols) is at maximum for $\psi=0^{\circ}$, decreases towards 45° and has a second maximum at 90°. In crossed polarization (open symbols) we find a fourfold symmetry for the ψ dependence of the scattering intensity. Both observations point to A_1. It is, however, remarkable that the intensity for parallel polarization of the incident and scattered light does not vanish for $\psi=45°$ as expected for A_1.[34] This is observed for the *xy* and *xz* surfaces of the crystal, but not on the *yz* surface, where the intensity of the peak drops below 5% of its maximum value. These observations exclude the possibility of describing the polarization dependence of the signal using a single Raman tensor.

To resolve the apparent contradiction between the measured Raman intensity and the symmetry imposed Raman tensors, we take another look at the x-ray structure of the crystal in Fig. 3. The unit cell includes two pairs of parallel molecules, with an angle of 74° between their main rota-

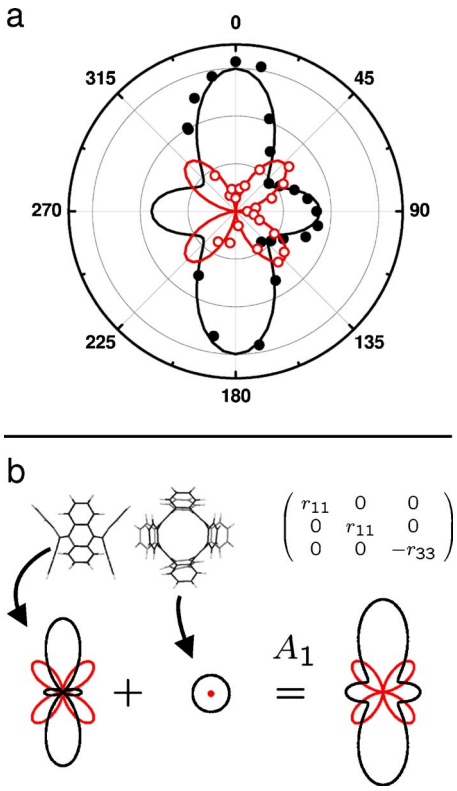

FIG. 7. (Color online) (a) Raman intensity of the peak at 1601 cm^{-1} vs angle ψ between the polarization of the incident light and the crystal y axis as defined in Fig. 6. The black closed circles correspond to parallel polarized incident and scattered light, the red (gray) open circles to perpendicularly polarized incident and scattered light. Lines are fits to our model for an A_1 vibration. (b) Proposed model for the unit cell for the Raman sample. The scattering pattern from each molecule is shown for an A_1 Raman tensor, as well as the sum, which corresponds to the expected intensity for independent scattering. Black lines correspond to parallel polarized incident and scattered light, red (gray) lines to perpendicularly polarized incident and scattered light.

tional axes. We now model the Raman intensity as the added contributions from two rotated molecules. This is justified because the atoms of two different picotubes in the crystal are at least separated by the typical van der Waals distance. Thus, we expect only a weak interaction between them. To explain the polarization dependence in Fig. 7(a) we assume a simplified crystal structure with two noninteracting perpendicular molecules as building blocks [see Fig. 7(b)]. This unit cell gives rise to a structure with two equivalent faces, in good agreement with our observation (see Fig. 6). We identify the equivalent faces as the xy and xz surfaces of our crystal. The third, different face, corresponds to yz. For such a crystal the Raman signal can be calculated as

$$I \propto (\mathbf{e}_i \cdot \mathcal{R}_{PT} \cdot \mathbf{e}_s)^2 + (\mathbf{e}_i \cdot \mathcal{R}_{PT}^{\perp} \cdot \mathbf{e}_s)^2, \qquad (2)$$

where $\mathcal{R}_{PT}$ is the Raman tensor of a picotube molecule and $\mathcal{R}_{PT}^{\perp}$ the same Raman tensor rotated by 90°. The form of the Raman tensors can be derived from group theory.[34]

In Fig. 7(b) we show the independent contribution of each molecule of the simplified unit cell for an A_1 Raman tensor

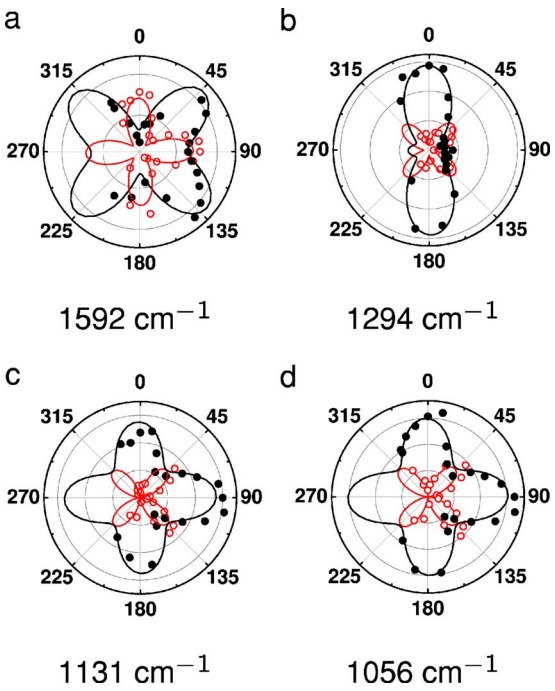

FIG. 8. (Color online) Raman intensity vs angle ψ between the polarization of the incident light and the y axis as defined in Fig. 6 for four picotube modes. The closed black circles correspond to parallel incident and scattered light, the open red (gray) circles to crossed incident and scattered light. (a) 1592 cm^{-1}. The fit corresponds to the sum of two modes with A_1 and E symmetry from two perpendicular, independent molecules according to Eq. (2). Measured ψ dependence for the modes at (b) 1294, (c) 1131, and (d) 1056 cm^{-1}. The fits correspond to the A_1 symmetry, plus a small B_2 component for the mode at 1294 cm^{-1}.

[Eq. (2)]. The resulting intensity in the weak-interaction approximation is the sum of the intensities for the independent molecules. Using Eq. (2) we obtain an excellent fit of the data for the mode at 1601 cm^{-1}, as can be seen in Fig. 7(a). We assign this peak to an A_1 mode.

Although the angle between the main rotational axes of the molecules in Fig. 3(a) slightly differs from 90°, this does not affect our conclusions. Modes with B_2 or E symmetry have their maxima at 45° for parallel polarized incident and scattered light. The functional form resulting from modes with B_1 symmetry is similar to those with A_1 on the xy side. However, on the zy surface the intensity from A_1 modes does not vanish, in contrast to our measurements for the 1601 cm^{-1} mode. Thus, A_1 is the only possible Raman tensor explaining the polarization of the 1601 cm^{-1} phonon of the picotube.

In Fig. 8(a) an equivalent plot is shown for the mode at 1592 cm^{-1}. It cannot be satisfactorily described by any of the symmetries of the D_{2d} group alone. However, it can be fitted as the superposition of intensities corresponding to two vibrational modes of similar frequency but different symmetries. From the functional form of the measured ψ dependence we find that one mode belongs to the A_1 or B_1 representations and the other one to B_2 or E. The fit in Fig. 8(a) includes an A_1 and an E Raman tensor. Panel (b) shows the data for the peak at 1294 cm^{-1}. The fit was performed

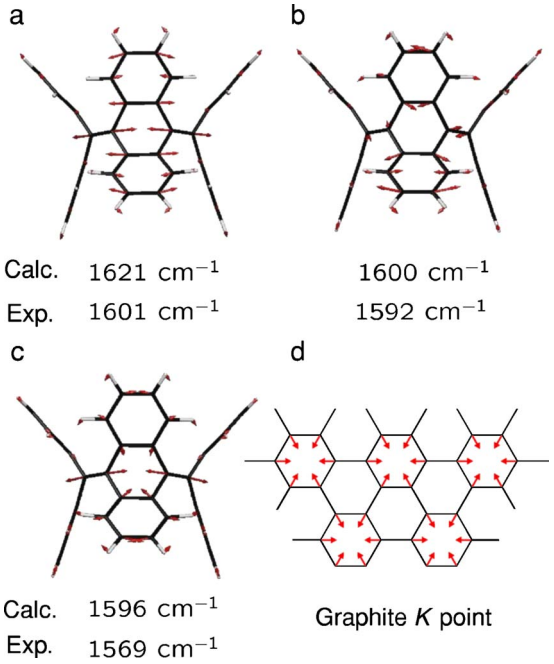

FIG. 9. (Color online) Calculated A_1 eigenvectors in the frequency range corresponding to the measured band at $\approx$1600 cm^{-1}. The calculated frequencies and the assigned experimental frequencies are indicated. The mode shown in panel (a) corresponds to the totally symmetric Raman active high-energy mode of armchair nanotubes, derived from the optical in-plane phonon of graphite. In panel (c) we show a vibrational mode related to the *K*-point TO mode of graphite [shown schematically in (d)]. The TO branch of graphite gives rise to the *D* mode.

with an A_1 Raman tensor, plus a very small B_2 component to account for the nonvanishing intensity at $\psi=0°$ for the crossed configuration. Panels (c) and (d) of Fig. 8 show further data and fits of two different modes. Panel (c) can be assigned to the A_1 symmetry using the information from the *zy* surface as we did for the mode at 1601 cm^{-1}. The mode shown in Fig. 8(d) is of A_1 or B_1 symmetry.

The modes at 1158 and 1171 cm^{-1} behave similarly to the 1294 cm^{-1} mode [Fig. 8(b)]. The modes at 1066 and 1042 cm^{-1} show intensity plots similar to the one shown in Fig. 8(d). In Table III the fitted elements of the Raman tensors are summarized, normalized to r_{11} of the peak at 1600 cm^{-1}.

C. *Ab initio* calculations

From the Raman measurements shown in the previous sections we obtained the frequencies and symmetries of the vibrational modes of the picotube molecules in the crystal. To assign the measured modes to atomic displacement patterns, we performed *ab initio* calculations of the vibrational modes of the picotube molecule. We found 32 pure C-H stretching modes with frequencies between 3088 and 3165 cm^{-1}. Below these frequencies, the first mode appears at 1643 cm^{-1}.

Around 1600 cm^{-1} we find three A_1 modes in our calculation with frequencies 1596, 1600, and 1621 cm^{-1}. The eigenvectors are shown in Figs. 9(a)–9(c). The mode at 1621 cm^{-1} is clearly related to the Γ-point high-energy mode of armchair carbon nanotubes.[39] As we discussed in Sec. V B, the measured band must contain more than three modes with different symmetries. In the frequency region between 1596 and 1621 cm^{-1} we find nine further C-C stretching eigenvectors with tangential displacements perpendicular to the picotube axis like those shown in Fig. 9 with B_1 (one mode), B_2 (two modes), and E symmetries (three pairs of eigenvectors). We will call these modes transversal. Above them we find eight eigenvectors, all of them with tangential displacements mainly along the picotube axis (longitudinal). Their symmetries are A_2 (two modes), B_1 (two modes), and E (two pairs of eigenvectors). We conclude that the eigenvectors underlying the measured peaks in the high-energy region are most likely transversal C-C stretching modes.

The eigenvector shown in Fig. 9(c) is related to the *K* point transverse optical phonon of graphite [Fig. 9(d)].[31] Rolling the graphene sheet in Fig. 9(d) to a nanotube we obtain a totally symmetric eigenvector. Correspondingly we expect a totally symmetric equivalent for the picotube. After searching all A_1 picotube eigenvectors we find the mode at 1596 cm^{-1} resembles most the graphite mode [see Fig. 9(c)]. The corresponding phonon branch of graphite gives rise to the so-called defect-induced mode or *D* mode.[2,38,45] In graphite and carbon nanotubes the *D*-mode frequency shifts with laser excitation energy, which had been a Raman puzzle for more than 20 years.[52] This behavior was finally explained by double-resonant Raman process involving phonons close to the *K* point of graphite.[38] Recent measurements of the phonon dispersion of graphite[53] yielded a frequency of 1265 cm^{-1} for the *D*-mode branch at the *K* point, much lower than expected from *ab initio* calculations.[54] The low frequency of the phonon branch was explained by the large electron-phonon coupling of the mode to the Fermi electrons in graphite (Kohn anomaly).[53,55] The atomic displacement opens a gap at the Fermi level, lowering the total energy of the system. This results in a softening of the phonon frequency. In the picotubes the *D*-like mode is much higher in frequency (1596 cm^{-1}) than in graphite or carbon nanotubes ($\approx$1350 cm^{-1} for excitations in the visible energy range). This is in excellent agreement with the Kohn-anomaly picture, because the picotube is a semiconductor without electronic states at the Fermi energy.

In the region around 1445 cm^{-1}, we find several modes combining C-C stretching and C-C-H bending, in which mainly the atoms in the wings move. In particular, we find two A_1 modes at 1450 and 1456 cm^{-1} in good agreement with the measured frequencies. The mode at 1456 cm^{-1} is shown in Fig. 10(a). The second mode shows an identical displacement pattern but only for the *o* wings.

We identify the measured A_1 peak at 1294 cm^{-1} as the calculated A_1 vibration at 1290 cm^{-1} [see Fig. 10(b)]. The main effect of this displacement pattern is to stretch the bonds 2*i* and 2*o* [see Fig. 2(b)]. As discussed in Sec. III A these bonds have lengths and display an angle typical for an sp^3 hybridization. The stretching of these bonds gives rise to a frequency which is fairly close to the diamond frequency of 1332 cm^{-1}. Around the measured frequency of 1238 cm^{-1}, we find several sp^3-like C-C stretch modes.

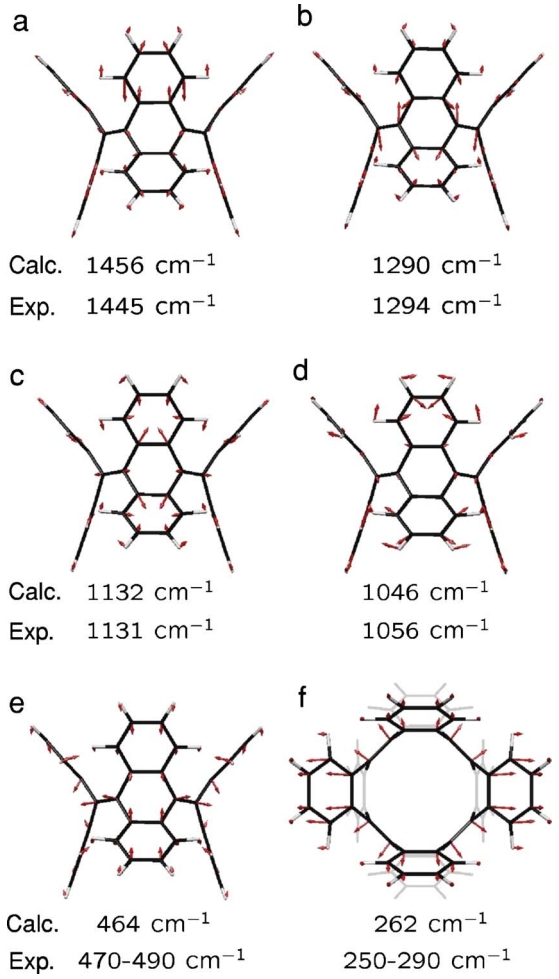

FIG. 10. (Color online) Selected calculated eigenvectors, calculated frequencies, and assigned experimental frequencies. They all belong to the A_1 representation. Gray carbon-carbon bonds in (f) are in the background (displacement omitted for clarity).

At lower frequencies, we found only two modes that are not of A_2 symmetry and hence Raman active: a B_1 mode at 1157 cm^{-1} and an E mode at 1163 cm^{-1}. The measurements yield modes at 1158 and 1171 cm^{-1} in good agreement with the calculated frequencies. However, the measured A_1 symmetry cannot be explained by the calculations. Our calculations yield an eigenvector with A_1 symmetry and energy 1136 cm^{-1} [see Fig. 10(c)] which can be identified with the intense peak at 1131 cm^{-1}. As we showed in Sec. V B, the symmetry of three modes measured at 1066, 1056, and 1042 cm^{-1} is either A_1 or B_1. Looking at the calculations, we find three modes with these symmetries: a B_1 mode at 1040 cm^{-1}, an A_1 mode at 1047 cm^{-1} shown in Fig. 10(d), and a B_1 mode at 1047 cm^{-1}. The next mode with one of these symmetries appears at 1076 cm^{-1}.

The group of modes measured around 480 cm^{-1} are related to the radial-breathing mode of carbon nanotubes. In the *ab initio* calculation we find several wing-torsion modes at 494 cm^{-1} and above, and mixed radial-axial modes at 475 cm^{-1} and below. In Fig. 10(e) we show the A_1 radial-axial eigenvector with frequency 466 cm^{-1}. Mixing of the radial-breathing mode with the axial-translation branch is found in the phonon dispersion of carbon nanotubes. For $q \neq 0$ these two branches have the same symmetry. They show a level anticrossing and interchange their eigenvectors with a strong mixing in the intermediate region. The mode calculated at 466 cm^{-1} is analogous to such a mixed radial-axial eigenmode.

In the low-energy region, we find mainly radial modes. The following eigenvectors are in very good agreement with the measured frequencies: the *wing-hexagon bending* at 287 cm^{-1}, the *ring-hexagon libration* at 253 cm^{-1}, and a breathing mode at 267 cm^{-1} [see Fig. 10(f)]. As explained in Sec. V, the frequency of this mode is softened with respect to the RBM frequency of carbon nanotubes [see Eq. (1)]. The reason for this frequency softening is the lower symmetry of the picotubes. In carbon nanotubes, all atoms are equivalent by symmetry. Therefore, the magnitude of the atomic displacements must be constant for an A_{1g} phonon like the radial-breathing mode. In the picotube, there are eleven nonequivalent atoms, which relaxes the symmetry constraints on the A_{1g} displacements. Since the breathinglike mode in Fig. 10(f) is not purely radial, several C-C bonds are not stretched resulting in a lowering of the frequency.

VI. CONCLUSIONS

We presented a thorough theoretical and experimental study of the physical properties of picotube molecules and crystals. We found the measured crystal structure to be almost identical to the calculated structure of an isolated molecule. This, together with the large distance between the molecules in the crystal, implies a low molecular interaction. The atoms in the central ring of the molecule show an angle of 109°, typical of sp^3 hybridization. This confirms the curvature-related rehybridization of σ and π orbitals in carbon nanotubes. The calculated picotube density of states shows a gap of 2.3 eV, in contrast to the metalicity of the (4,4) nanotube. However, the symmetries of the HOMO and LUMO are analogous in both systems.

We presented polarization-dependent Raman experiments on the three inequivalent sides of picotube crystals. The spectrum is dominated by a feature at 1601 cm^{-1}. The shape of this mode is very similar to that of the high-energy modes of single-walled nanotubes. In the picotube, several modes of different symmetry form this band, including the characteristic sp^2 vibration related to the optical in-plane phonon of graphite. We assigned the symmetry of the most intense peaks, in most cases A_1. Comparing with *ab initio* calculations of the vibrations of an isolated picotube we identified most of the measured modes, and in particular those corresponding to nanotube modes: the high-energy mode, the D mode, and the radial-breathing mode.

In conclusion, we showed strong analogies between the physical properties of picotube molecules and single-walled carbon nanotubes, but also interesting additional features. We benefited from the knowledge about carbon nanotubes in order to understand the similarities to picotubes, and learn about effects caused by the differences between these two compounds.

ACKNOWLEDGMENTS

We thank P. Ordejón for his valuable help, U. Kuhlmann for the symmetry analysis tool, B. Schöler for the technical support, and P. Rafailov and M. Tommasini for helpful discussions. S.R. was supported by the Oppenheimer Fund and Newnham College. We acknowledge the Ministerio de Ciencia y Tecnología (Spain) and the Deutsche Akademische Austausch Dienst (Germany) for a Spanish-German Research action. This work was partially supported by the DFG under Grant No. Th662/8-2.

[1] S. Kammermeier, P. G. Jones, and R. Herges, Angew. Chem., Int. Ed. Engl. **35**, 2669 (1996); S. Kammermeier, P. G. Jones, and R. Herges, Angew. Chem. **108**, 2834 (1996).

[2] S. Reich, C. Thomsen, and J. Maultzsch, *Carbon Nanotubes, Basic Concepts and Physical Properties* (Wiley-VCH, Berlin, 2004).

[3] J. W. Mintmire and C. T. White, Carbon **33**, 893 (1995).

[4] J. Kürti, V. Zólyomi, M. Kertesz, and G. Sun, New J. Phys. **5**, 125 (2003).

[5] S. M. Bachilo, M. S. Strano, C. Kittrel, R. H. Hauge, R. E. Smalley, and R. B. Weisman, Science **298**, 2361 (2002).

[6] H. Telg, J. Maultzsch, S. Reich, F. Hennrich, and C. Thomsen, Phys. Rev. Lett. **93**, 177401 (2004).

[7] Y. Miyauchi, S. Chiashi, Y. Murakami, Y. Hayashida, and S. Maruyama, Chem. Phys. Lett. **387**, 198 (2004).

[8] S. Reich, C. Thomsen, and J. Robertson, Phys. Rev. Lett. **95**, 077402 (2005).

[9] N. Wang, Z. K. Tang, G. D. Li, and J. S. Chen, Nature (London) **408**, 50 (2000).

[10] N. Wang, G. D. Li, and Z. K. Tang, Chem. Phys. Lett. **339**, 47 (2001).

[11] M. J. López, I. Cabria, N. H. March, and J. A. Alonso, Carbon **43**, 1371 (2005).

[12] Z. M. Li *et al.*, Phys. Rev. Lett. **87**, 127401 (2001).

[13] M. Machón, S. Reich, C. Thomsen, D. Sánchez-Portal, and P. Ordejón, Phys. Rev. B **66**, 155410 (2002).

[14] H. J. Liu and C. T. Chan, Phys. Rev. B **66**, 115416 (2002).

[15] I. Cabria, J. W. Mintmire, and C. T. White, Phys. Rev. B **67**, 121406(R) (2003).

[16] X. Blase, L. X. Benedict, E. L. Shirley, and S. G. Louie, Phys. Rev. Lett. **72**, 1878 (1994).

[17] S. Reich, C. Thomsen, and P. Ordejón, Phys. Rev. B **65**, 155411 (2002).

[18] C. Fantini, A. Jorio, M. Souza, M. S. Strano, M. S. Dresselhaus, and M. A. Pimenta, Phys. Rev. Lett. **93**, 147406 (2004).

[19] V. N. Popov, New J. Phys. **6**, 17 (2004).

[20] See EPAPS Document No. E-PRBMDO-72-132535 for a crystallographic information file (cif). This document can be reached via a direct link in the online article's HTML reference section or via the EPAPS homepage (http://www.aip.org/pubservs/epaps.html).

[21] Dilor spectrometer, model LABRAM. HORIBA Jobin Yvon SAS, Longjumeau, France.

[22] P. Ordejón, E. Artacho, and J. M. Soler, Phys. Rev. B **53**, R10441 (1996).

[23] J. M. Soler, E. Artacho, J. D. Gale, A. García, J. Junquera, P. Ordejón, and D. Sánchez-Portal, J. Phys.: Condens. Matter **14**, 2745 (2002).

[24] J. P. Perdew and A. Zunger, Phys. Rev. B **23**, 5048 (1981).

[25] N. Troullier and J. L. Martins, Phys. Rev. B **43**, 1993 (1991).

[26] J. Junquera, O. Paz, D. Sánchez-Portal, and E. Artacho, Phys. Rev. B **64**, 235111 (2001).

[27] R. Herges, M. Deichmann, J. Grunenberg, and G. Bucher, Chem. Phys. Lett. **327**, 149 (2000).

[28] C. Castiglioni, M. Tommasini, and G. Zerbi, Philos. Trans. R. Soc. London, Ser. A **362**, 2425 (2004).

[29] Y. L. Mao, X. H. Yan, Y. Xiao, J. Xiang, Y. R. Yang, and H. L. Yu, Nanotechnology **15**, 1000 (2004).

[30] J. P. Perdew and M. Levy, Phys. Rev. Lett. **51**, 1884 (1983).

[31] C. Mapelli, C. Castiglioni, G. Zerbi, and K. Müllen, Phys. Rev. B **60**, 12710 (1999).

[32] M. Damnjanović, T. Vuković, and I. Milošević, Solid State Commun. **116**, 265 (2000).

[33] T. Inui, Y. Tanabe, and Y. Onodera, *Group Theory and its Application in Physics* (Springer-Verlag, Berlin, 1996).

[34] M. Cardona, in *Light Scattering in Solids II*, edited by M. Cardona and G. Güntherodt, Topics in Applied Physics Vol. 50 (Springer, Berlin, 1982), p. 19.

[35] M. Paillet, P. Poncharal, A. Zahab, J.-L. Sauvajol, J. C. Meyer, and S. Roth, Phys. Rev. Lett. **94**, 237401 (2005).

[36] G. S. Duesberg, I. Loa, M. Burghard, K. Syassen, and S. Roth, Phys. Rev. Lett. **85**, 5436 (2000).

[37] C. Thomsen, S. Reich, P. M. Rafailov, and H. Jantoljak, Phys. Status Solidi B **214**, R15 (1999).

[38] C. Thomsen and S. Reich, Phys. Rev. Lett. **85**, 5214 (2000).

[39] J. Maultzsch, S. Reich, and C. Thomsen, Phys. Rev. B **65**, 233402 (2002).

[40] J. Maultzsch, S. Reich, U. Schlecht, and C. Thomsen, Phys. Rev. Lett. **91**, 087402 (2003).

[41] L. X. Benedict, S. G. Louie, and M. L. Cohen, Phys. Rev. B **52**, 8541 (1995).

[42] H. Ajiki and T. Ando, Jpn. J. Appl. Phys., Suppl. **34-1**, 107 (1994).

[43] S. Reich, C. Thomsen, G. S. Duesberg, and S. Roth, Phys. Rev. B **63**, 041401(R) (2001).

[44] H. H. Gommans, J. W. Alldredge, H. Tashiro, J. Park, J. Magnuson, and A. G. Rinzler, J. Appl. Phys. **88**, 2509 (2000).

[45] S. Reich and C. Thomsen, in *Raman Spectroscopy in Carbons: From Nanotubes to Diamond*, edited by A. C. Ferrari and J. Robertson, special issue of Philos. Trans. R. Soc. London, Ser. A **362**, 2271 (2004).

[46] C. Thomsen, S. Reich, and J. Maultzsch, in *Raman Spectroscopy in Carbons: From Nanotubes to Diamond* (Ref. 45), p. 2337.

[47] E. Dobardžić, I. Milošević, B. Nikolić, T. Vuković, and M. Damnjanović, Phys. Rev. B **68**, 045408 (2003).

[48] R. A. Jishi, L. Venkataraman, M. S. Dresselhaus, and G. Dresselhaus, Chem. Phys. Lett. **209** 77 (1993).

[49] J. Kürti, G. Kresse, and H. Kuzmany, Phys. Rev. B **58**, R8869

(1998).

[50] D. Sánchez-Portal, E. Artacho, J. M. Soler, A. Rubio, and P. Ordejón, Phys. Rev. B **59**, 12678 (1999).

[51] We use the Porto notation [T. C. Damen, S. P. S. Porto, and B. Tell, Phys. Rev. **142**, 570 (1966)] to indicate the measurement geometry: $\mathbf{k}_i(\mathbf{e}_i\mathbf{e}_s)\mathbf{k}_s$ where $\mathbf{k}_{i(s)}$ indicates the propagation direction of the incident (scattered) light and $\mathbf{e}_{i(s)}$ the direction of the polarization of the incident (scattered) light.

[52] R. P. Vidano, D. B. Fischbach, L. J. Willis, and T. M. Loehr, Solid State Commun. **39**, 341 (1981).

[53] J. Maultzsch, S. Reich, C. Thomsen, H. Requardt, and P. Ordejón, Phys. Rev. Lett. **92**, 075501 (2004).

[54] O. Dubay and G. Kresse, Phys. Rev. B **67**, 035401 (2003).

[55] S. Piscanec, M. Lazzeri, F. Mauri, A. C. Ferrari, and J. Robertson, Phys. Rev. Lett. **93**, 185503 (2004).